Cite this paper as: I*norg. Chem.*, **2018**, *57*, 8465-8475, DOI: acs.inorgchem.8b01147

Kinetico-mechanistic study of the redox pH cycling processes occurring on a robust water soluble cyanido-bridged mixed valence $\{Co^{III}/Fe^{II}\}_2$ square

Laura Alcázar,[a] *Paul V. Bernhardt,*[b] *Montserrat Ferrer,*[a] *Mercè Font-Bardia,*[c] *Albert Gallen,*[a] *Jesús Jover,*[a] *Manuel Martínez,*[*a] *Jack Peters*[a] *and Timothy J. Zerk*[b]

[a] Departament de Química Inorgànica i Orgànica, Secció de Química Inorgànica, Universitat de Barcelona, Martí i Franquès 1-11, E-08028 Barcelona, Spain.
e-mail: manel-martinez@qi.ub.es

[b] School of Chemistry and Molecular Biosciences, University of Queensland, Brisbane 4072, Queensland, Australia

[c] Unitat de Difracció de RX, Centres Científics i Tecnològics de la Universitat de Barcelona (CCiTUB), Universitat de Barcelona, Solé i Sabarís 1-3, E-08028-Barcelona, Spain

ABSTRACT

A kinetico-mechanistic study of reversible electron transfer processes undergone by the water soluble, cyanide bridged mixed-valence $[\{Co^{III}\{(Me)_2(\mu\text{-ET})cyclen\}\}_2\{(\mu\text{-NC})_2Fe^{II}(CN)_4\}_2]^{2-}$ square has been carry out. The oxidation reaction consists of a two-step process with the participation of a solvent-assisted outer-sphere complex, as a result of the establishment of hydrogen bonds that involve the oxo groups of the oxidant (peroxodisulfate) and the terminal cyanido ligands of the tetrametallic square. The reduction reaction of the fully oxidised ($[\{Co^{III}\{(Me)_2(\mu\text{-ET})cyclen\}\}_2\{(\mu\text{-NC})_2Fe^{III}(CN)_4\}_2]$) core, which produces H_2O_2 from H_2O even at low pHs, is also a two-step process. Each one of these processes requires a set two pre-equilibria involving in the association of OH^- and its subsequent deprotonation by a further of OH^- anion.

The structure of the square compound in its fully protonated form has been also determined by XRD and shows the existence of rather strong hydrogen interactions, in agreement with the rather high basicity of the terminal cyanido ligands. Likewise, DFT calculations on the tetrametallic complex showed zones with negative electrostatic potential around the Fe^{II} centres of the square that would account for the establishment of the hydrogen bonds found in the solid state. Spectroelectrochemistry experiments demonstrated the singular stability of the $\{Co^{III}/Fe^{III}\}^{2-}$ complex, as well as that of their partially, $\{Co_2^{III}/Fe^{III}Fe^{II}\}^-$, and fully oxidised $\{Co^{III}/Fe^{III}\}$ counterparts, since no hysteresis was observed in these measurements.

Introduction

Self-assembly of macrocyclic metal complexes is a powerful method for the construction of well-defined architectures with interesting structure-specific properties such as guest recognition, optical and/or magnetic properties or multiredox behaviour among many others.[1-3] Given the fact that a large variety of metallamacrocycles are built with redox-active transition metal fragments as corners and/or redox-active ligands as linkers, it is rather surprising that the number of studies that specifically aim at taking advantage of that inherent property are still rather limited. Nevertheless, in recent years there has been a growing interest in these redox- active species due to their potentially interesting properties (optical, magnetic, catalytic activity, molecular recognition, etc.). Published comprehensive reports[4,5] provide examples of electro-active metallic assemblies whose redox activity is localized in the organic ligands and/or the metallic corners.

Although the number of examples containing redox-active bridging ligands (based on units such as tetrathiafulvalene or perylene bisimide) or blocking ligands (bearing moieties such as ferrocenyl) is much larger than that including redox-active metal corners, some macrocycles containing Cu^{II}/Cu^{III}, Co^{II}/Co^{III} and Co^{III}/Co^{IV}, Fe^{II}/Fe^{III}, Ru^{II}/Ru^{III} or Mo^{II}/Mo^{III} as redox active pairs have been reported.[6-10] Surprisingly, these reports lack of any reference to discrete Prussian blue species, although these compounds usually display redox activity due to the presence of Fe and/or Co multiple valence ions.[11] Nevertheless, an increasing number of interesting examples of Prussian blue molecular polymetallic assemblies have been reported due to the fact that they usually exhibit both optical and magnetic bistability which arises from a reversible metal-to metal charge transfer between the Co^{III} (or Fe^{III}) and the Fe^{II} centres. This family of compounds include pentanuclear trigonal bipyramidal $\{Fe^{II}_2/Fe^{III}_3\}$ and $\{Fe^{II}_2/Co^{III}_3\}$ units,[12,13] octanuclear cubic $\{Fe^{II}/Fe^{III}\}_4$ and $\{Fe^{II}/Co^{III}\}_4$ assemblies,[14,15] homonuclear $\{Fe^{II}/Fe^{III}\}_2$ squares, [16,17] and a significant number of heterotetranuclear square complexes $\{Fe^{II}/Co^{III}\}_2$.[11,18,19]

Recently, we have reported the preparation of the diamagnetic cyanido-bridged $[\{Co^{III}\{(Me)_2(\mu\text{-ET})cyclen\}\}_2\{(\mu\text{-NC})_2Fe^{II}(CN)_4\}_2]^{2-}$ square complex[20] *via* a mechanistically designed self-assembly reaction (Scheme 1). The process involves a rate limiting outer-sphere redox reaction followed by a fast substitution/inner-sphere redox reaction sequence that had been studied by us for some time.[21-28] Although this compound did not show any evidence of complete intramolecular electron transfer phenomena, its striking stability in aqueous solution (stable across the full aqueous pH range, in deep contrast with that of other reported redox active metallomacrocycles), opens up the possibility of performing a thorough study of its participation in chemical processes, such as reversible oxidation, protonation, and OH^- association.

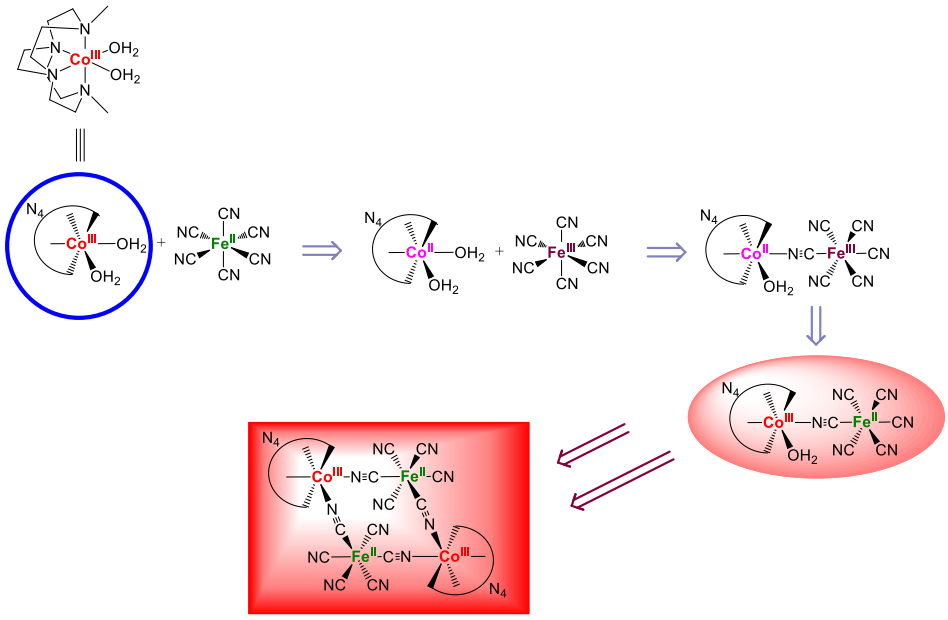

Scheme 1.- Mechanistic process involved in the preparation of the cyanido-bridged $[\{Co^{III}\{(Me)_2(\mu\text{-}ET)cyclen\}\}_2\{(\mu\text{-}NC)_2Fe^{II}(CN)_4\}_2]^{2-}$ square complex of this study.

With these facts in mind, we are here reporting a redox-reversible kinetico-mechanistic study of our tetrametallic $\{Fe^{II}/Co^{II}\}_2$ unit as a function of pH, oxidant concentration, temperature and pressure. In addition, a study of the charge distribution of the fully reduced species and the *mono*- and *bis*-oxidized forms by DFT calculations has been carried out in order to rationalize our experimental observations. The results indicate an extremely robustness of the square unit in all the aqueous pH range, as well as a keystone contribution from outer-sphere recognition due to hydrogen bonding interactions, as a consequence of the participation of solvation water molecules, which display a different behaviour/actuate in a way that can not be attributed to mere electrostatic effects. These features allow considering the complexes studied as having a rather versatile multi-redox chemistry with implications in electrochromism.

Results and Discussion

Crystal structure of $(H_3O)_2[\{Co^{III}\{(Me)_2(\mu\text{-}ET)cyclen\}\}_2\{(\mu\text{-}NC)_2Fe^{II}(CN)_4\}_2].4HClO_4.9H_2O$

Even though the central core of the title compound has already been inferred *via* several techniques,[20] the solid-state structure of the cores had not been possible to obtain. Nevertheless, the knowledge of the protonation and redox properties of the core has enabled us to design a way to produce the compound in a much more insoluble fashion that could be crystallised.

Caramel-coloured crystals of the title complex were obtained by slow concentration of a 1M $HClO_4$ solution of the parent compound $Na_2[\{Co^{III}\{(Me)_2(\mu\text{-}ET)cyclen\}\}_2\{(\mu\text{-}NC)_2Fe^{II}(CN)_4\}_2]$ at 4 °C. The structure contains centrosymmetric cyanide-bridged $\{Fe_2(\mu\text{-}CN)_4Co_2\}$units bearing a nearly planar square-shaped geometry, in which the Co and Fe ions are alternately bridged by cyanide ions. The anion structure together with selected bond distances and bond angles are shown in Figure 1a.

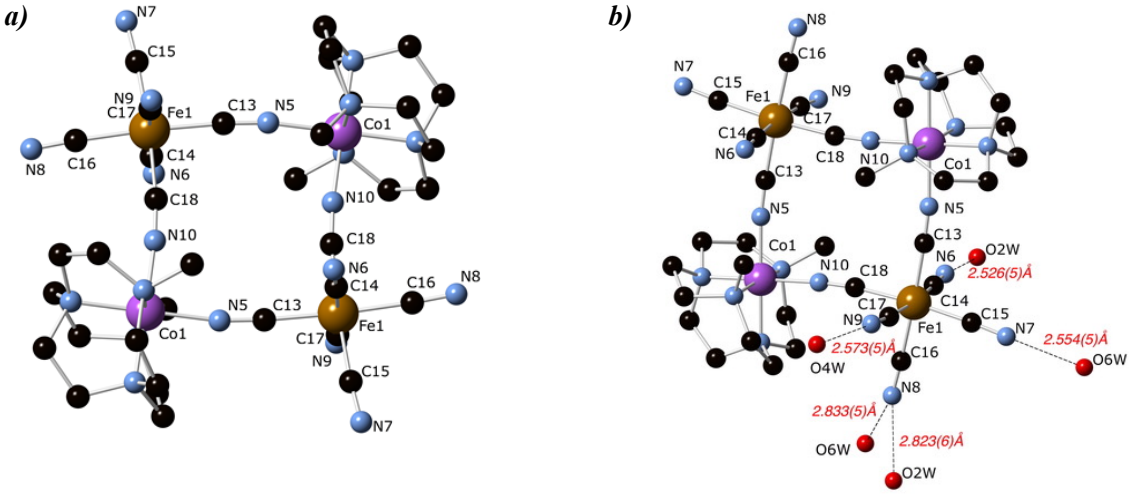

Figure 1.- X-ray crystal structure of *$(H_3O)_2[\{Co^{III}\{(Me)_2(\mu\text{-}ET)cyclen\}\}_2\{(\mu\text{-}NC)_2Fe^{II}(CN)_4\}_2].4HClO_4.9H_2O$*. ***a)*** Square unit of the mixed-valence complex, hydrogen atoms, solvent and counterions are omitted for clarity. Selected bond lengths (Å) and angles (º): Co(1)-N(10) 1.910(3), Co(1)-N(5) 1.919(3), Co(1)-N(2) 1.925(3), Co(1)-N(3) 1.935(3), Co(1)-N(1) 1.981(3), Co(1)-N(4) 1.989(3), Fe(1)-C(17) 1.880(4), Fe(1)-C(14) 1.885(4), Fe(1)-C(15) 1.896(4), Fe(1)-C(18) 1.902(4), Fe(1)-C(13) 1.910(4), Fe(1)-C(16) 1.921(4). N(10)-Co(1)-N(5) 88.82(13), C(18)-Fe(1)-C(13) 90.50(15), C(18)-N(10)-Co(1) 173.2(3), N(10)-C(18)-Fe(1) 173.5(3), C(13)-N(5)-Co(1) 171.8(3), N(5)-C(13)-Fe(1) 176.0(3). ***b)*** Part of the extensive 3D network found in the structure, showing the variety of hydrogen-bond lengths.

The distances between adjacent iron and cobalt centres through the cyanide linkers are very similar (4.936(2) and 4.956(2) Å) and the angles Fe1-Co1-Fe1 and Co1-Fe1-Co1 are 88.47(1) and 91.53(1) º, respectively thus displaying a regular square macrocyclic core, in good agreement with other reported

examples of squares containing {Co^{III}-CN- Fe^{II}} edges.[18,19,29-35] The coordination bond lengths about the Co ion are in the range of 1.910(3)-1.989(3) Å, characteristic of LS Co^{III} ions.[13] The Fe-C distances are within 1.880(4) and 1.921(4) Å, confirming the LS character of the Fe ions present in the compound.[32,33] The total compound charge , as well as the absence of an LMCT (Fe^{III}-CN) band in the electronic spectrum are in agreement with Fe^{II} centres in the complex.

In addition to the discrete tetranuclear metal units $[\{Co^{III}\{(Me)_2(\mu\text{-ET})cyclen\}\}_2\{(\mu\text{-}NC)_2Fe^{II}(CN)_4\}_2]^{2-}$, perchlorate anions, hydronium cations and lattice water molecules are also found in the crystal packing. The anionic squares are stacked forming columns along the b axis (Figure S1) with an angle of 57.4 ° between the planes of consecutive macrocycles. Moreover, a complex 3D network is formed as a result of the establishment of extensive hydrogen-bonding interactions that involve the oxygen atoms of lattice water molecules, H_3O^+ cations, and ClO_4^- anions and the nitrogen atoms of all the terminal cyanido ligands (Figure 1b). Interestingly, three of these interactions are singularly strong (O2W···N6 =2.526(5), O6W···N7 =2.554(5) and O4W···N9=2.573(5)) Å in comparison with those reported for analogous square $\{Co^{III}Fe^{II}\}_2$ compounds in agreement with the basic character exhibited by the terminal CN groups of the compound.[30,32,36]

Spectroelectrochemistry: redox stability

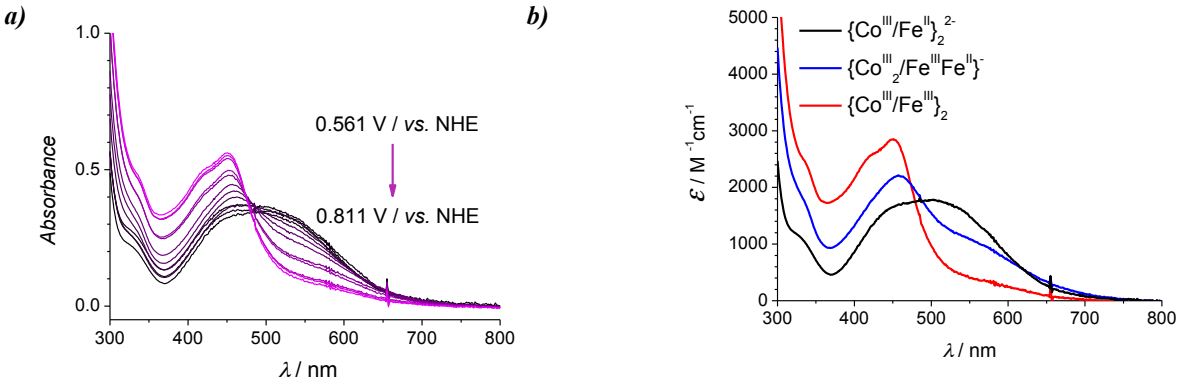

Figure 2.- a) Spectroelectrochemistry of a 2.0×10^{-3} M solution of $\{Co^{III}/Fe^{II}\}_2^{2-}$ in H_2O (pH = 7.0, I = 0.1 M $LiClO_4$). Platinum flag working electrode, Ag/AgCl/sat. NaCl reference electrode, platinum wire counter electrode. Cell pathlength = 1.0 mm. b) ReactLab calculated spectra of the fully oxidized $\{Co^{III}/Fe^{III}\}_2$, fully reduced $\{Co^{III}/Fe^{II}\}_2^{2-}$ and intermediate $\{Co^{III}_2/Fe^{III}Fe^{II}\}^-$ complexes; aqueous solution, pH 7, I = 0.1M $LiClO_4$, $E_{Fe(II)/Fe(III)(1)}$ = 0.628 V, $E_{Fe(III)/Fe(III)(2)}$ = 0.7322 V *versus.* NHE.

We previously measured the cyclic voltammetry of the title complex in aqueous solution and showed that it exhibits two discrete $Fe^{II/III}$ redox couples.[20] Both $Fe^{II/III}$ redox couples are reversible which indicates that the complex is stable in each of the fully oxidised $Fe^{III}Fe^{III}$, fully reduced $Fe^{II}Fe^{II}$ and intermediate $Fe^{III}Fe^{II}$ forms, while the $Co^{II/III}$ redox couples being irreversible under the same conditions. Herein we measured the spectroelectrochemistry of the complex at pH 7.00 poising the potential at increasingly positive potentials (oxidation) and then returning incrementally to the starting

potential (reduction). At each poised potential the observed spectrum was stable for a minimum of one hour and no hysteresis was observed in the spectra of the oxidation and reduction sweeps (Figure S2) which testifies to the remarkable stability of the complex. Simulating the data from Figure 2a using ReactLab Redox allowed us to determine the redox potentials exactly and also revealed the spectrum of the intermediate $Fe^{III}Fe^{II}$ complex (Figure 2b, blue curve).The separation of the two $Fe^{III/II}$ couples ($\Delta E > 100$ mV) is much larger than that expected for two non-interacting Fe centres ($2RT/F \ln 2 = 35.6$ mV)[37] which shows that the charge increase at the oxidised Fe centre influences the redox potential of the other Fe centre thus raising its redox potential.

DFT calculations

In view of the feasibility of pursuing the kinetico-mechanistic studies of the reversible redox processes indicated in Figure 2, and given the fact that the $\{Co^{III}/Fe^{II}\}_2^{2-}$ core is extremely robust, some DFT calculations have been conducted in order to investigate the possible differences among the $\{Co^{III}/Fe^{II}\}_2^{2-}/\{Co^{III}_2/Fe^{III}Fe^{II}\}^{-}/\{Co^{III}/Fe^{III}\}_2$ triad that could explain the reactivity observed.

The above indicated structures were optimized with DFT calculations using the crystal structure of the $\{Co^{III}/Fe^{II}\}_2^{2-}$ core as starting point (the detailed procedure is described in the Experimental section). From the calculations, the oxidation process does not entail major changes in the structure; the central square unit of the $\{Co^{III}Fe^{II}\}_2^{2-}$ complex remains practically the same with Fe…Co, Fe…Fe and Co…Co distances of 4.99, 6.93 and 7.20 Å, respectively. These values are very similar to those found in the crystal structure, where the average Fe…Co separation is 4.95 Å while the Fe…Fe and Co…Co distances are 6.90 and 7.09 Å. In the same line, the computed Fe…Co…Fe and Co…Fe…Co angles are close to those in the crystal structure: 87.8 *versus* 88.5 ° and 92.2 *versus* 91.5 °, respectively. In all cases, as in the determined crystal structure, the four metals remain in same plane and the octahedral $Fe(CN)_6$ units show an eclipsed arrangement, with twist angles between iron hexacyanido units always below 0.5 °. The consecutive oxidation of the $\{Co^{III}Fe^{II}\}_2^{2-}$ complex produces open-shell species with one unpaired electron in the oxidised iron centres. For the half oxidised $\{Co^{III}_2/Fe^{III}Fe^{II}\}^{-}$ species, the unpaired electron is localized on the new Fe^{III} centre (Figure 3a), while for the fully oxidized $\{Co^{III}/Fe^{III}\}_2$ complex the species can be either a triplet or an open-shell singlet; in practice, both possibilities have practically the same energy and display very similar structures. All the results appearing throughout this manuscript are referred to the open-shell singlet $\{Co^{III}/Fe^{III}\}_2$ complex. As in the $\{Co^{III}_2/Fe^{II}Fe^{III}\}^{-}$ species, the electron spin density remains localized on the Fe^{III} centres (Figure 3b).

The Molecular Electrostatic Potential (MEP) maps show the formal charge distribution of the total electron density of the complexes, *i.e.* the regions with charge depletion and accumulation that can be used to explain the reactivity and bonding of chemical species (Figure 4). As expected, the positively

charged areas are always located around the cobalt centres while the iron surroundings are more negative in all species. The maximum and minimum surface charge values vary accordingly to the total charge of the complexes, *i.e.* red to light blue surface for $\{Co^{III}/Fe^{II}\}_2^{2-}$, orange to blue for $\{Co^{III}{}_2/Fe^{III}Fe^{II}\}^-$ and green to dark blue for $\{Co^{III}/Fe^{III}\}_2$ in Figure 4. The MEP map of $\{Co^{III}/Fe^{II}\}_2^{2-}$ clearly reflects the bonding found in the crystal structure, where the square tetrametallic core interacts with H_3O^+ through hydrogen bonding of the terminal, negatively charged, cyanido ligands bound to the iron centres. The different Fe^{II} and Fe^{III} atoms in $\{Co^{III}{}_2/Fe^{III}Fe^{II}\}^-$ can be clearly distinguished with the MEP map; the former is located in a zone with negative electrostatic potential (orange, Figure 4b top) while the latter belongs to a space where the surface charge is more postive (yellow, Figure 4b bottom).

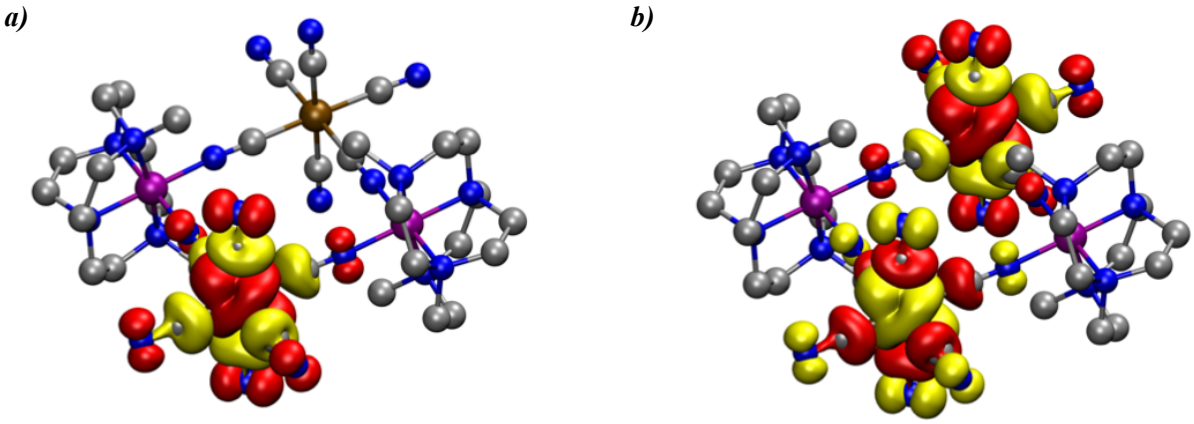

Figure 3.- Electron spin densities computed for complexes: a) $\{Co^{III}{}_2/Fe^{III}Fe^{II}\}^-$; b) $\{Co^{III}/Fe^{III}\}_2$ (color code: C = gray, N = blue, Fe = brown, Co = purple, H atoms have been omitted for clarity).

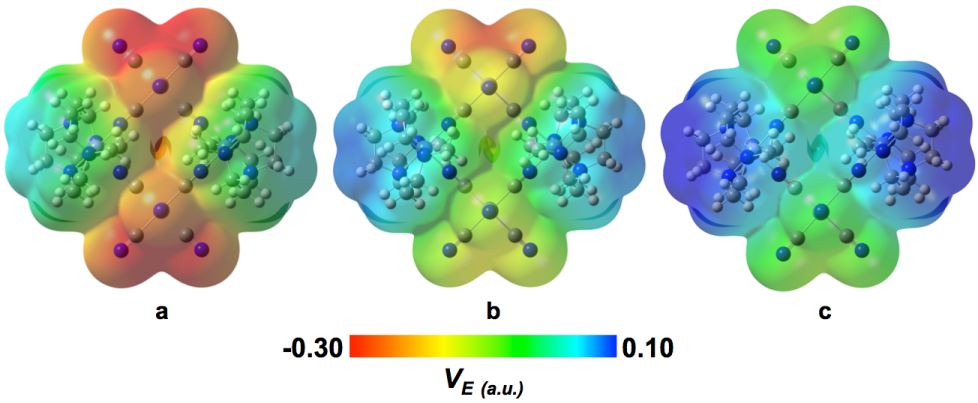

Figure 4.- MEP maps on the 0.002 isosurfaces of: a) $\{Co^{III}Fe^{II}\}_2^{2-}$; b) $\{Co^{III}{}_2/Fe^{III}Fe^{II}\}^-$; c) $\{Co^{III}Fe^{III}\}_2$ (red and blue colors represent negative and positive values of electrostatic potential (V_E)).

The $\{Co^{III}/Fe^{III}\}_2$ complex reacts with hydroxide to produce hydrogen peroxide and the reduced $\{Co^{III}/Fe^{II}\}_2^{2-}$ species (see below). The experimental data indicate that this is an outer-sphere redox process. Nevertheless, the small size of the OH^- anion could suggest an encapsulation of the anion in the central cavity of the tetranuclear metallic core prior to the electron transfer. This hypothesis has been tested by optimizing a $\{Co^{III}/Fe^{III}\}_2$–OH^- species in which the hydroxide anion is placed in the geometrical centre of the cavity. After the optimization the hydroxide group is observed to migrate to the external part of the complex, where it can interact with the dangling methyl groups of the cyclen ligand. As the metal centres surrounding the cavity do not exert any stabilizing effect on the incoming OH^- group, a mechanism where the hydroxo groups are inside the cavity would be expected.

Kinetics of the oxidation reaction of the $\{Co^{III}/Fe^{II}\}_2^{2-}$ complex

The oxidation reaction of simpler but related $(Co^{III}/Fe^{II})^-$ mixed-valence dinuclear complexes, sodium μ-cyanido-1κ*N*:2κ*C*-(2-methyl-tetraazaciclo-amine)-1κ^5*N*-pentacyanido-2κ^5*C*-(1-cobalt(III)-1-ferrate(II)),with peroxodisulfate has been already studied, and the behaviour has been explained as an initial one-electron oxidation of Fe^{II} to Fe^{III} producing SO_4^{2-} and $SO_4^{\cdot-}$ followed by a fast (non rate-determining) second one-electron process involving the $SO_4^{\cdot-}$ radical.[24,28,38,39]

In view of the spectroelectrochemical data shown above, as well as the redox non-equivalence of the two iron centres,[20] the oxidation of the new $\{Co^{III}/Fe^{II}\}_2^{2-}$ mixed-valence square was pursued from a kinetico-mechanistic perspective at varying concentrations of peroxodisulfate, pH, temperature and pressure. As collected in Table S1, in all cases the time-resolved spectra agree with the operation of a two step consecutive process in the acidity range between pH = 8.5 and 1 M $HClO_4$. Furthermore, the Specfit or ReactLab -calculated spectra[40,41] of the intermediate compound agrees very well with that of the single electron oxidised $\{Co^{III}{}_2/Fe^{III}Fe^{II}\}^-$ mixed valence compound determined from the spectroelectrochemical measurements (see Figure 2 and S3). Figure 5 collects an example of the trends observed for the two pseudo-first order rate constants derived (k_{obs1} and k_{obs2}) with the concentration of oxidant.

By comparison with our previous data on $(Co^{III}/Fe^{II})^-$ dinuclear complexes the reaction can be explained by the sequence shown in Scheme 2, which produces a rate law such as that indicated in Equation 1 for both rate-determining reaction steps.[42-44] Nevertheless, it is clear that for the observation of the second step in the reaction sequence (*ox2a* and *ox2b*), the $SO_4^{\cdot-}$ radical generated by the first oxidation step (*ox1a* and *ox1b*) has to react preferentially with the excess of reducing $\{Co^{III}/Fe^{II}\}_2^{2-}$ to further produce $\{Co^{III}{}_2/Fe^{III}Fe^{II}\}^-$ intermediate (*oxf1*) . Any other option would make the reaction sequence show a single rate determining step behaviour.

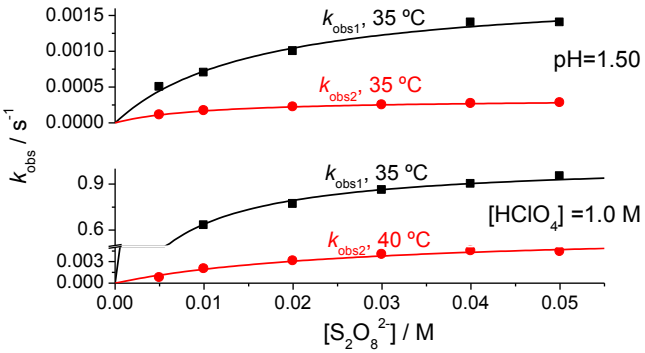

Figure 5.- Plot of the values of the first order rate constants, k_{obs}, for the two step $S_2O_8^{2-}$ oxidation of the $\{Co^{III}/Fe^{II}\}_2^{2-}$ mixed-valence square at different temperatures and acidities.

$$k_{obs} = \frac{k_{ox}\, K_{OS}\, [S_2O_8^{2-}]}{1 + K_{OS}[S_2O_8^{2-}]}$$

Equation 1

$$\{Co^{III}/Fe^{II}\}_2^{2-} + S_2O_8^{2-} \overset{K_{OS1}}{\rightleftharpoons} \{\{Co^{III}/Fe^{II}\}_2^{2-};S_2O_8^{2-}\} \qquad ox1a$$

$$\{\{Co^{III}/Fe^{II}\}_2^{2-};S_2O_8^{2-}\} \xrightarrow{k_{ox1}} \{Co^{III}_2/Fe^{III}Fe^{II}\}^{-} + SO_4^{2-} + SO_4^{\cdot-} \qquad ox1b$$

$$\{Co^{III}_2/Fe^{III}Fe^{II}\}^{-} + S_2O_8^{2-} \overset{K_{OS2}}{\rightleftharpoons} \{\{Co^{III}_2/Fe^{III}Fe^{II}\}^{-};S_2O_8^{2-}\} \qquad ox2a$$

$$\{\{Co^{III}_2/Fe^{III}Fe^{III}\}^{-};S_2O_8^{2-}\} \xrightarrow{k_{ox2}} \{Co^{III}/Fe^{III}\}_2 + SO_4^{2-} + SO_4^{\cdot-} \qquad ox2b$$

$$\{Co^{III}/Fe^{II}\}_2^{2-} + SO_4^{\cdot-} \xrightarrow{fast} \{Co^{III}_2/Fe^{III}Fe^{II}\}^{-} + SO_4^{2-} \qquad oxf1$$

$$\{Co^{III}_2/Fe^{III}Fe^{II}\}^{-} + SO_4^{\cdot-} \xrightarrow{fast} \{Co^{III}/Fe^{III}\}_2 + SO_4^{2-} \qquad oxf2$$

SCHEME 2

From the curvature shown in the plots, it is clear that both k_{obs} rate constants show the typical limiting behaviour obtained for outer-sphere redox processes where the formation of the precursor outer-sphere complex (K_{OS}) is dominant.[43] Although this effect had not previously been observed for oxidations by $S_2O_8^{2-}$, the reaction of the dinuclear $(Co^{III}/Fe^{II})^{-}$ species with $[Co^{III}(oxalate)_3]^{3-}$ effectively showed this behaviour. Important interactions in the outer-sphere precursor complex had been established as responsible of this fact.[23,39]

From the limiting value obtained from fitting the data to Equation 1, the values of k_{ox} and K_{OS} at different temperatures and acidities can be derived for both reaction steps (*ox1* and *ox2*, Scheme 2). By measuring the temperature-dependence of k_{ox} and fitting the data to the Eyring equation (Figure 6a), the corresponding thermal activation parameters can be calculated for both electron transfer processes.[44] The pressure dependence of the values of k_{obs} at concentrations of $S_2O_8^{2-}$ at which the plot has practically reached saturation ($k_{ox} \approx k_{obs}$ at $[S_2O_8^{2-}]$=0.05-0.07 M) was also studied in order to determine the activation volumes of the two steps. Figure 6b shows some of the lnk_{ox} *versus P* plots at the pH where a definite neat oxidation is observed (see next section),[45] and Table 1 collects a summary of the equilibrium kinetic and activation data determined.

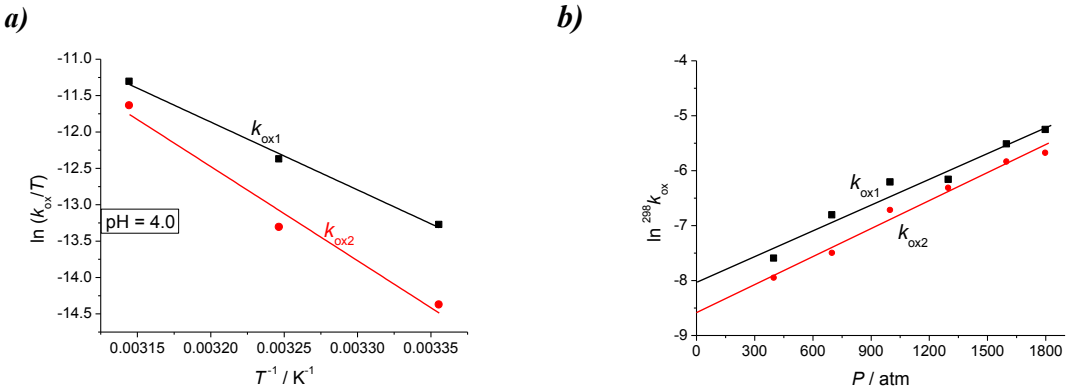

Figure 6.- a) Eyring plot for the variation of the values of k_{ox} for the two steps observed with temperature at pH= 4.0. b) lnk_{ox} *versus P* plot for the reaction carried out at pH = 2.0 and 25 ºC.

Table 1.- Thermal and pressure activation parameters for the two consecutive reaction steps observed in the oxidation of the $\{Co^{III}/Fe^{II}\}_2^{2-}$ mixed-valence square with $S_2O_8^{2-}$ at different pH values. The values of K_{OS} (according to Equation 1) are the average from the values at the different temperatures measured.

pH	K_{OS1} /M^{-1}	$^{298}k_{ox1}$ /s^{-1}	$\Delta H_{ox1}^{\ddagger}$ /kJ mol^{-1}	$\Delta S_{ox1}^{\ddagger}$ /J $K^{-1}mol^{-1}$	$\Delta V_{ox1}^{\ddagger}$ /cm^3mol^{-1}
8.5	70	1.3×10^{-3}	70±7	-90±20	n.d.
4.0	100	5.1×10^{-4}	80±8	-55±25	n.d.
1.5	90	3.8×10^{-4}	100±15	20±40	$-38\pm4_{(pH\ 2.0)}$
0	150	$0.62_{(293\ K)}$	20±5	-180±20	*ca.* 0
pH	K_{OS2} /M^{-1}	$^{298}k_{ox2}$ /s^{-1}	$\Delta H_{ox2}^{\ddagger}$ /kJ mol^{-1}	$\Delta S_{ox2}^{\ddagger}$ /J $K^{-1}mol^{-1}$	$\Delta V_{ox2}^{\ddagger}$ /cm^3mol^{-1}
8.5	30	1.8×10^{-4}	90±10	-30±30	n.d.
4.0	55	2.2×10^{-4}	90±6	-26±20	n.d.
1.5	40	2.0×10^{-4}	100±12	18±40	$-41\pm3_{(pH\ 2.0)}$
0	40	$1.2\times10^{-3}{}_{(293\ K)}$	80±10	-20±50	-5.2±0.8

Kinetics of the reduction reaction of the oxidised $\{Co^{III}/Fe^{III}\}_2$ complex

From our previous studies carried out on the simpler $(Co^{III}/Fe^{II})^-$ mixed-valence dinuclear complexes, a pH-dependent reversible redox process has been demonstrated.[24,39] Consequently, the reduction

process of the new $\{Co^{III}/Fe^{III}\}_2$ square (obtained by peroxodisulfate oxidation in acidic conditions of $\{Co^{III}/Fe^{II}\}_2^{2-}$)[20] in alkaline solutions to produce H_2O_2 was also studied from a kinetico-mechanistic perspective. Interestingly, for this new tetranuclear $\{Co^{III}/Fe^{III}\}_2$ compound the reduction process reverting to the mixed-valence $\{Co^{III}/Fe^{II}\}_2^{2-}$ square complex, with formation of hydrogen peroxide, is observed even at acidic pH values (the reaction is observed from pH = 3.0 upwards). As found for the previously described oxidation reaction by peroxodisulfate, the reduction process is clearly a two consecutive step sequence from the time resolved fitting of the full spectra by the standard software indicated in the experimental section.[41,42]

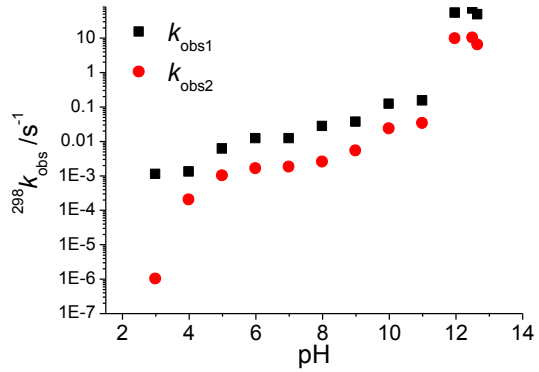

Figure 7.- Logarithm scale plot of the fast and slow rate constants for the two steps observed on the reduction of the $\{Co^{III}/Fe^{III}\}_2$ square with OH^- at different buffered pHs at 25 ºC ([square] ≈ 4×10^{-4} M; I = 1.0 M ($NaClO_4$)).

Figure 7 summarises the trends observed for the values of k_{obs1} and k_{obs2} with the concentration of OH^-. For the reduction of the simpler $(Co^{III}/Fe^{III})^-$ dinuclear complexes, two equilibrium processes involving the OH^- reductant precede the rate determining formation of peroxide; these are formation of an OH^- adduct, followed by its deprotonation by another OH^-. Thus an $[OH^-]^2$- dependence of the k_{obs} rate constants is observed.[39] In the present case this is not so, and a double titration plot is observed with pK_{eq} values within the 3-4 and 11-12 ranges. Table S2 collects all the values k_{obs} obtained under the different conditions of the study and Scheme 3 collects the reaction sequence that results from the data. In this scheme the values of k_{et1} and k_{et2} necessarily include the two equilibrium constants involving hydroxide which are in the above-mentioned range.

$$\{Co^{III}/Fe^{III}\}_2 + OH^- \xrightarrow{k_{et1}} \{Co^{III}{}_2/Fe^{III}Fe^{II}\}^- + OH^{\cdot}$$

$$\{Co^{III}{}_2/Fe^{III}Fe^{II}\}^- + OH^- \xrightarrow{k_{et2}} \{Co^{III}/Fe^{II}\}_2^{2-} + OH^{\cdot}$$

$$2\ OH^{\cdot} \xrightarrow{fast} H_2O_2$$

SCHEME 3

From the values obtained it is clear that the validity of the previous oxidation data collected at pH>3.0 have to be considered with caution as a faster reduction of the oxidised complex is occurring simultaneously in an approximately catalytic reaction. Probably the observed process corresponds *de facto* to and oxidation reaction, but once the buffer has been consumed.

In this respect cyclic voltammetry experiments were conducted at variable pH values in the range where a dramatic increase on the reduction rate constants is observed (7-13, Figure 7). The purpose of these measurements was to examine the possible occurrence of an electrochemically catalysed oxidation of OH^- to H_2O_2. Figure 8 shows that the fully reduced complex is reversibly oxidised in two discrete steps to the $\{Co^{III}/Fe^{III}Fe^{II}\}^-$ and $\{Co^{III}/Fe^{III}\}$ complexes at pH 7.0. However, at higher pHs the voltammetry is slightly perturbed and the peak oxidative current (i_{pa}) of the first wave increases slightly above pH 10. This behaviour is expected for an electrochemical oxidation coupled to a catalytic chemical reaction (Scheme S1, and confirms that hydroxide is only oxidized by $\{Co^{III}/Fe^{III}\}_2$ at an appreciable rate above pH 10 under the non-buffered experimental conditions used here. Two clarifications should be noted in relation to Figure 8. First, the non-specific oxidation of hydroxide by the electrode is only observed at very high potentials (> 0.85 V *vs* NHE) and is not responsible for the change in the peak anodic current (i_{pa}). Second, though the change in i_{pa} is small it is definitive; this is indicated by the stable baseline current during the initial oxidation sweep (*i.e.* the current at 0.4 V *vs* NHE is the same across the range of pH's during the initial sweep in the positive direction).

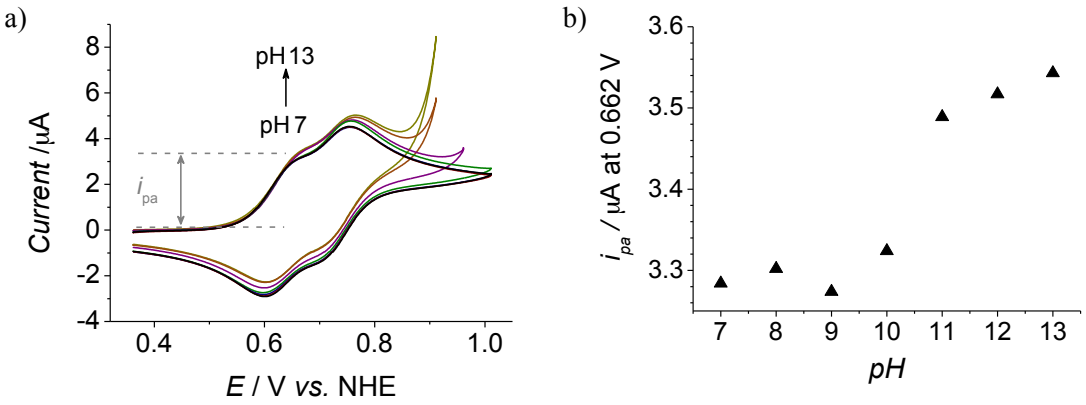

Figure 8.- a) pH-dependent voltammetry of a 7.3×10^{-4} M solution of $\{Co^{III}/Fe^{II}\}_2^{2-}$ in H_2O (I = 0.1 M $LiClO_4$. Scan rate = 10 mV s^{-1}. Potential initially swept in the positive direction. b) pH-dependence of the peak anodic current (i_{pa}) at 0.662 V.

Mechanism of the $\{Co^{III}/Fe^{II}\}_2^{2-}$ oxidation process

From the data collected a key difference emerges between the oxidation kinetics of the dianionic $\{Co^{III}/Fe^{II}\}_2^{2-}$ square complex and the parent monoanionc series of $(Co^{III}/Fe^{II})^-$ dinuclear species previously prepared by us. While for the mixed-valent monoanionic $(Co^{III}/Fe^{II})^-$ dinuclear complexes the build-up of outer-sphere precursor complexes with peroxodisulfate (according to Equation 1) is minimal, in the present case the equilibrium constants, K_{OS}, indicated in Scheme 2 are large enough for the observation of limiting kinetics in both consecutive oxidation reaction rate-determining steps (Table 1 and Figure 5).[43] In the previous studies with the $(Co^{III}/Fe^{II})^-$ dinuclear species, the only time this behaviour was observed was when $[Co(oxalate)_3]^{3-}$ was used as oxidant, despite the unfavourable increase in charge repulsion.[39] This fact was attributed to a solvent-assisted nature of the outer-sphere complex formed, which was also thoroughly described for similar $[Co(oxalate)_3]^{3-}$ reactivity.[46] It is thus clear that in the present case an outer-sphere solvent-assisted encounter complex is formed with $S_2O_8^{2-}$, both with the dianionic $\{Co^{III}/Fe^{II}\}_2^{2-}$ and monoanionic $\{Co^{III}_2/Fe^{III}Fe^{II}\}^-$ species in the first and second rate-determining reaction steps, respectively. Furthermore, the fact that the *ox2a* and *ox2b* reaction step is observed in the oxidation process (Scheme 2), despite the possible operation of reaction *oxf2*, indicates that the solvent-assisted outer-sphere complex formed in *ox1a* involves solely one of the oxo groups of peroxodisulfate, thus liberating the resulting $SO_4^{\cdot-}$ radical to the reaction medium. In this way a two electron oxidation process is not operative, and the liberated radical can react both with $\{Co^{III}/Fe^{II}\}_2^{2-}$ and $\{Co^{III}_2/Fe^{III}Fe^{II}\}^-$ ensuring the observation of the second step (*ox2a* and *ox2b*, Scheme 2) of the full process (Scheme 4).

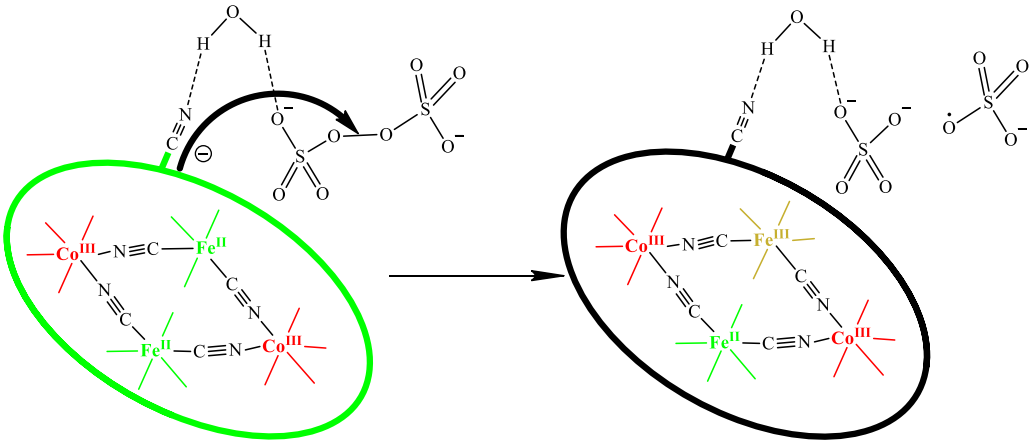

SCHEME 4

In this respect, from the valid data in Table 1 (*i.e.* pH values of 1.5, 2.0 and 0, see previous section and Figure 7), it is also clear that the values of K_{OS} decrease by *ca.* half on going from the $\{Co^{III}/Fe^{II}\}_2^{2-}$ to the $\{Co^{III}{}_2/Fe^{III}Fe^{II}\}^-$ complexes, opposite to that expected considering the electrostatics involved; clearly some other factor has to be dominant. The only possibility to come to terms with this fact relates precisely again with the existence of a solvent-assisted outer-sphere complexation where water is more tightly bound to more anionic complexes.[47-49] Nevertheless, when the fully protonated $H_2\{Co^{III}/Fe^{II}\}_2$ species is considered (pH = 0) the trend is maintained with equivalent (if not larger) values of K_{OS}, thus implying that the outer-sphere solvent-assisted complexation should occur on the non-protonated nitrile units; even simultaneous hydrogen-bonding between a molecule of water with the non-protonated and protonated nitrile units can explain these facts (Scheme 4 and S2).[50,51]

As for the kinetic and activation parameters at pH >2.0 (see Table 1), there is a dramatic change on going from the single (pH =1.5-2.0) to the doubly protonated mixed-valence square complex (pH = 0). The first step of the oxidation reaction (k_{ox1}) is accelerated by a factor of 10^3 while the second step rate constant undergoes only a 10-fold increase. These values are clearly related to the thermal activation $\Delta H^{\neq}$ and $\Delta S^{\neq}$ values, which indicate a much higher degree of association in the transition state and a lower enthalpy demand on decreasing pH (both effects being more pronounced for the first rate-determining step of the oxidation reaction). Interestingly, the oxidation potential of the Fe^{II} centres becomes more positive on protonation,[20,24] which would be expected to produce higher enthalpy demands. Again, the proper association of the oxidant and reductant *via* a solvent molecule should be held responsible of the acceleration found (*vide supra*). As for the volumes of activation, these show opposite trends to $\Delta S^{\neq}$, in agreement with the operation of hydrogen-bonding interactions in the transition state and are mostly related to desolvation of the complexes as found for similar systems.[47,48,52]

Mechanism of the $\{Co^{III}/Fe^{III}\}_2$ reduction process

Data shown in Figure 7 clearly indicate that, although the value of the reduction potential increases with decreasing pH, the trend observed for the rate constants measured for both reaction steps (Scheme 3) is opposite. Previously studied similar reactions on (Co^{III}/Fe^{III}) dinuclear complexes[39,53] indicated that the formation of an outer-sphere OH^- aggregate and its further deprotonation by a second OH^- group agree with the data obtained; a $[OH^-]^2$-dependence was observed for the values of k_{obs}. In the present study such a trend is not observed and, although in the pH range between 5 and 10 the increase of both k_{et1} and k_{et2} is practically linear, the values increase dramatically on going to pH 11 to reach a final plateau. Increasing the acidity to pH = 3 produces an opposite immediate decrease of the second step rate constant and a build-up of the $\{Co^{III}{}_2/Fe^{III}Fe^{II}\}^-$ intermediate complex; further increase in acidity makes both reduction processes too slow to be observed.

From these data it is clear that outer-sphere involvement of OH^- with the oxidised $\{Co^{III}/Fe^{III}\}_2$ square complex plays a crucial role in its reduction to the mixed-valence parent species and the formation of H_2O_2. In this respect it is interesting to note that the aggregation of hydroxide with the reduced $\{Co^{III}/Fe^{II}\}_2^{2-}$ has already been established by UV-Vis spectroscopy.[20] Furthermore, the pH values where dramatic changes in rate constants are observed can be easily associated with the deprotonation of a coordinated water molecule (pK_a around 3-5) or of a coordinated hydroxide (pK_a around 9-12).[54] With all these facts in mind, we propose the reaction sequence shown in Scheme 5 as responsible for the trends observed. From the data in Figure 7 the values of pK_{dep1} and pK_{dep2} both are found equivalent and within the 11-12 range; as expected due to the fact that the values of K_{dep} are directly associated with the deprotonation of a $\{Fe^{III}\cdot OH^-\}$ adduct in reactions *red1a* and *red2b* (Scheme 5). Furthermore, compound $\{\{Co^{III}/Fe^{III}\}_2\cdot H_2O\}$ is expected to be more acidic than $\{\{Co^{III}{}_2/Fe^{III}Fe^{II}\}^-\cdot H_2O\}$ as effectively shown by the value of K_{add} (pK_{add1} being one unit lower than pK_{add2}; 2-3 *versus* 3-4). As a whole, the process is rather similar to the one established for the oxidation of the dinuclear (Co^{III}/Fe^{II}) parent mixed-valence complexes. For present complexes, though, the higher acidity on the initial $\{Co^{III}/Fe^{III}\}_2$ oxidised square allows for the full dissociation of the initial adduct, even at high pHs. Furthermore, the difference between the acidities of the $\{\{Co^{III}/Fe^{III}\}_2\cdot H_2O\}$ and $\{\{Co^{III}{}_2/Fe^{III}Fe^{II}\}^-\cdot OH^-\}$ (or the half reduced intermediate species) allows for a full separation of the effects of K_{add} and K_{dep} for the reaction sequence indicated in Scheme 5.

$$\{\{Co^{III}/Fe^{III}\}_2\cdot H_2O\} + OH^- \underset{}{\overset{K_{add1}}{\rightleftharpoons}} \{\{Co^{III}{}_2/Fe^{III},Fe^{III}\}\cdot OH^-\} + H_2O \qquad \textit{red1a}$$

$$\{\{Co^{III}{}_2/Fe^{III},Fe^{III}\}\cdot OH^-\} + OH^- \underset{}{\overset{K_{dep1}}{\rightleftharpoons}} \{\{Co^{III}{}_2/Fe^{III},Fe^{III}\}\cdot O^{2-}\} + H_2O \qquad \textit{red1b}$$

$$\{\{Co^{III}{}_2/Fe^{III},Fe^{III}\}\cdot O^{2-}\} \xrightarrow{k_{red1}} \{\{Co^{III}{}_2/Fe^{III},Fe^{II}\}^-\cdot O^-\} \qquad \textit{red1c}$$

$$\{\{Co^{III}{}_2/Fe^{III},Fe^{II}\}^-\cdot O^-\} \xrightarrow{fast} \{Co^{III}{}_2/Fe^{III},Fe^{II}\} + O^- \qquad \textit{redf1}$$

$$\{\{Co^{III}{}_2/Fe^{III},Fe^{II}\}^-\cdot H_2O\} + OH^- \underset{}{\overset{K_{add2}}{\rightleftharpoons}} \{\{Co^{III}{}_2/Fe^{III},Fe^{II}\}^-\cdot OH^-\} + H_2O \qquad \textit{red2a}$$

$$\{\{Co^{III}{}_2/Fe^{III},Fe^{II}\}\cdot OH^-\} + OH^- \underset{}{\overset{K_{dep2}}{\rightleftharpoons}} \{\{Co^{III}{}_2/Fe^{III},Fe^{II}\}^-\cdot O^{2-}\} + H_2O \qquad \textit{red2b}$$

$$\{\{Co^{III}{}_2/Fe^{III},Fe^{II}\}^-\cdot O^{2-}\} \xrightarrow{k_{red2}} \{\{Co^{III}/Fe^{II}\}_2{}^{2-}\cdot O^-\} \qquad \textit{red2c}$$

$$\{\{Co^{III}/Fe^{II}\}_2{}^{2-}\cdot O^-\} \xrightarrow{fast} \{Co^{III}/Fe^{II}\}^{2-}{}_2 + O^- \qquad \textit{redf2}$$

$$2\ O^- \xrightarrow{fast} O_2^{2-}$$

$$O_2^{2-} + H_2O \underset{}{\overset{K_a^{-1}}{\rightleftharpoons}} O_2H^- + OH^-$$

SCHEME 5

Conclusions

The structure of the heterotetranuclear cyanido-bridged square-shaped $[\{Co^{III}\{(Me)_2(\mu\text{-}ET)cyclen\}\}_2\{(\mu\text{-}NC)_2Fe^{II}(CN)_4\}_2]^{2-}$ mixed-valence complex has been unambiguously established by X-ray diffraction in its fully protonated form; the structure shows extensive hydrogen-bonding interactions with water molecules, H_3O^+, and the nitrogen atoms of the terminal cyanido ligands. Spectroelectrochemical measurements indicate that the stability of the complex, as well as that of their partially, $\{Co_2^{III}/Fe^{III}Fe^{II}\}^-$, and fully oxidised $\{Co^{III}/Fe^{III}\}$ counterparts is remarkable, in accordance with the absence of hysteresis observed in these measurements. DFT calculations have been also been conducted, and the results agree with the surprising stability and robustness of the square $\{Co^{III}Fe^{II}\}_2^{2-}$ complex core in any of its oxidised forms. In this respect *Molecular Electrostatic Potential* maps support the establishment of possible hydrogen bonds between water and the terminal cyanido ligands. In all the remarkably robustness displayed opens up the possibility of studying its participation in a wide range of chemical processes in aqueous solution.

In this respect, the kinetico-mechanistic study of the two-step sequential oxidation reaction of the $\{Co^{III}/Fe^{II}\}_2^{2-}$ square with peroxodisulfate features a striking difference with the previously reported oxidation reaction of monoanionic $(Co^{III}/Fe^{II})^-$ dinuclear species. For the oxidation reaction of this anionic tetranuclear square-shaped complex, the actuation of outer-sphere water-assisted encounter complex involving an oxo group of peroxodisulfate anion is evident. The activation parameters are in agreement with the existence of these hydrogen-bonding interactions in the transition state.

Reduction by water of the fully oxidised $\{Co^{III}/Fe^{III}\}_2$ square, producing H_2O_2, occurs even at acidic pHs and, according to the interpretation of the kinetico-mechanistic results obtained, require the existence of two equilibrium processes previous to the rate determining step. These involve the existence of an OH^- adduct, either with $\{Co_2^{III}/Fe^{III}Fe^{II}\}^-$ or $\{Co^{III}/Fe^{III}\}$, and its subsequent deprotonation by another OH^- before the rate determining generation of hydrogen peroxide.

Clearly, a fine-tuning of the building block redox potentials *via* ligand design should expand the current study to further chemically robust polynuclear mixed-valence compounds. This robustness, the goal being including that of the Co^{III} centres on reduction, should provide discrete polynuclear molecules with very interesting electron transfer properties.

Experimental

General

The $\{Co^{III}/Fe^{II}\}_2^{2-}$ square mixed valence compound has been prepared following the procedures already described in the literature;[20] UV-Vis, ICP and cyclic voltammetry has been used as characterisation techniques.

Solution of the above complex in 1.0 M $HClO_4$ followed by long standing in the cool cabinet produced some aggregates of XRD-quality crystals that were subsequently used for the purpose.

Buffer solutions were prepared using the standard procedures for the pH values between the 3.0>pH<11; out of that range $HClO_4$ or NaOH solutions were used as effective buffers. In al cases the concentration of the buffer was at least 10-fold that of the reactants and the ionic strength was set at 1.0 with $NaClO_4$.[55,56]

DFT calculations

All the density functional theory (DFT) calculations have been carried out using water a solvent (PCM, see below) with the Gaussian09 (rev. D.01)[57] electronic structure package with a 10^{-8} convergence criterion for the density matrix elements, using the hybrid functional B3LYP.[58-60] The standard 6-31G* basis set[61-63] is used for all H, C, N and O atoms while the Stuttgart basis set (SDD),[61,64] including the associated ECP to describe the core electrons, has been employed for Fe and Co. Ultrafine integration grids have been used in all calculations to ensure a satisfactory convergence. In all cases the solvation energies are computed in water with the (IEF-PCM) continuum dielectric solvation model[65,66] using the SMD radii and non-electrostatic terms.[67] The dispersion correction terms have been included in all the calculations by using the D3 method of Grimme.[68] The vibrational analysis has been performed for all the computed structures to ensure the nature of the stationary, which have zero imaginary frequencies.

X-Ray Structure Analysis

A caramel prism-like specimen of $C_{36}H_{74}Cl_4Co_2Fe_2N_{20}O_{27}$, approximate dimensions 0.178 mm x 0.198 mm x 0.477 mm, was used for the X-ray crystallographic analysis. The X-ray intensity data were measured on a D8 Venture system equipped with a multilayer monochromator and a Mo microfocus (λ = 0.71073 Å). The frames were integrated with the Bruker SAINT software package[69] using a narrow-frame algorithm. The integration of the data using a monoclinic unit cell yielded a total of 126100 reflections to a maximum θ angle of 30.58 ° (0.70 Å resolution), of which 98435 were independent (average redundancy 12.811, completeness = 99.6 %, R_{int} = 5.80%, R_{sig} = 2.83 %) and 8040 (81.67%) were greater than $2\sigma(F^2)$. The final cell constants of a = 28.454(6) Å, b = 10.644(2) Å, c = 21.226(4) Å, α = 90.00(3) °, β = 91.14(3) °, γ = 90.00(3) °,

volume = 6427.(2) $Å^3$, are based upon the refinement of the XYZ-centroids of reflections above 20 σ(I). Data were corrected for absorption effects using the multi-scan method (SADABS).[70] The calculated minimum and maximum transmission coefficients (based on crystal size) are 0.6550 and 0.7461.

The structure was solved and refined using the Bruker SHELXTL Software Package,[71] using the space group C 1 2/c 1, with Z = 4 for the formula unit, $C_{36}H_{74}Cl_4Co_2Fe_2N_{20}O_{27}$. The final anisotropic full-matrix least-squares refinement on F^2 with 446 variables converged at R1 = 6.19 %, for the observed data and wR2 = 15.52 % for all data. The goodness-of-fit was 1.124. The largest peak in the final difference electron density synthesis was 1.322 $e^-/Å^3$ and the largest hole was -1.061 $e^-/Å^3$ with an RMS deviation of 0.209 $e^-/Å^3$. On the basis of the final model, the calculated density was 1.644 g/cm^3 and F(000), 3280 e^-. Table S3 collects the relevant data for the diffraction.

Electrochemistry

Electrochemistry experiments were carried out with a BioLogic SP-150 instrument using a glassy carbon working electrode, a Ag/AgCl (3 M KCl) reference electrode and platinum wire counter electrode on 1×10^{-3} M solutions of the sample and using 0.1 M $NaClO_4$ as supporting electrolyte, unless otherwise stated.

Spectroelectrochemistry experiments were carried out with the same instrument and the same standard setup in a CHI cell in a HP8453 UV-Vis spectrophotometer.

Kinetics

The kinetic profiles for the reactions at ambient pressure with were followed by UV-Vis spectroscopy in the 700-300 nm range on HP8452A or Cary50 instruments equipped with thermostated multicell transports. Runs with $t_{1/2}$<10 s were performed using an Applied Photophysics SX20 MV Stopped-flow instrument with photo-diode array detection (J&M TIDAS). For runs carried out at elevated pressures with $t_{1/2}$>10 s an already described pressurizing cell system setup was used connected to a TIDAS J&M instrument.[47] For experiments run at variable pressure with $t_{1/2}$<10 s, a previously described pressurised stopped-flow mixing unit was used that was connected with fibre optics to a J&M TIDAS instrument.[72]

Observed rate constants were derived from absorbance versus time traces at the wavelengths where a maximum increase and/or decrease of absorbance were observed. The calculation of the observed rate constants from the absorbance *versus* time monitoring of reactions, studied under first order concentration conditions, were carried out using the SPECFIT or ReactLab software packages;[40,41] the general kinetic technique is that previously described.[39,73] All post-run fittings were carried out by the standard available commercial programs.

For the oxidation reactions, solutions of the square compound were prepared in the relevant buffers at I =1.0 M ($NaClO_4$) and mixed with the relevant amount of peroxodisulfate buffered (I =1.0 M ($NaClO_4$)) stock solution and buffer at I = 1.0 M $NaClO_4$. For the reduction process the oxidised square was dissolved in 0.001 M $HClO_4$ and this was added to the relevant buffered solutions for the study (I = 1.0 M $NaClO_4$).

Acknowledgements Financial support from the Spanish Ministerio de Economía y Competitividad CTQ2015-65707C2-1/FEDER is acknowledged.

REFERENCES

[1] R. Chakrabarty, P. S. Mukherjee, P. J. Stang. *Chem. Rev.* **2011**, *111*, 6810-6918.

[2] H. Vardhan, M. Yusubov, F. Verpoort. *Coord. Chem. Rev.* **2016**, *306*, 171-194.

[3] S. Zarra, D. M. Wood, D. A. Roberts, J. R. Nitschke. *Chem. Soc. Rev.* **2015**, *44*, 419-432.

[4] C. H. M. Amijs, G. P. M. van Klink, G. van Koten. *Dalton Trans.* **2006**, 308-327.

[5] V. Croue, S. Goeb, M. Salle. *Chem. Commun.* **2015**, *51*, 7275-7289.

[6] P. D. Beer, N. Berry, M. G. B. Drew, O. D. Fox, M. E. Padilla-Tosta, S. Patell. *Chem. Commun.* **2001**, 199-200.

[7] H. T. Chifotides, I. D. Giles, K. R. Dunbar. *J. Am. Chem. Soc.* **2013**, *135*, 3039-3055.

[8] M. H. Chisholm, N. J. Patmore, C. R. Reed, N. Singh. *Inorg. Chem.* **2010**, *49*, 7116-7122.

[9] F. Fabrizi de Biani, M. Corsini, P. Zanello, H. Yao, M. E. Bluhm, R. N. Grimes. *J. Am. Chem. Soc.* **2004**, *126*, 11360-11369.

[10] T. Matsumoto, G. N. Newton, T. Shiga, S. Hayami, Y. Matsui, H. Okamoto, R. Kumai, Y. Murakami, H. Oshio. *Nature Communications* **2014**, *5*, 3865.

[11] D. Aguila, Y. Prado, E. S. Koumousi, C. Mathoniere, R. Clerac. *Chem. Soc. Rev.* **2016**, *45*, 203-224.

[12] M. Shatruk, A. Dragulescu-Andrasi, K. E. Chambers, S. A. Stoian, E. L. Bominaar, C. Achim, K. R. Dunbar. *J. Am. Chem. Soc.* **2007**, *129*, 6104-6116.

[13] C. P. Berlinguette, A. Dragulescu-Andrasi, A. Sieber, H. U. Güdel, C. Achim, K. R. Dunbar. *J. Am. Chem. Soc.* **2005**, *127*, 6766-6779.

[14] M. Nihei, M. Ui, N. Hoshino, H. Oshio. *Inorg. Chem.* **2008**, *47*, 6106-6108.

[15] D. Li, R. Clèrac, O. Roubeau, E. Harté, C. Mathonière, R. Le Bris, S. M. Holmes. *J. Am. Chem. Soc.* **2008**, *130*, 252-258.

[16] A. Mondal, Y. Li, P. Herson, M. Seuleiman, M. L. Boillot, E. Riviere, M. Julve, L. Rechignat, A. Bousseksou, R. Lescouezec. *Chem. Commun.* **2012**, *48*, 5653-5655.

[17] C. Zheng, J. Xu, F. Wang, J. Tao, D. Li. *Dalton Trans.* **2016**, *45*, 17254-17263.

[18] M. Nihei, Y. Yanai, I. J. Hsu, Y. Sekine, H. Oshio. *Angew. Chem. , Int. Ed.* **2017**, *56*, 591-594.

[19] S. De, J. R. Jimenez, Y. Li, L. M. Chamoreau, A. Flambard, Y. Journaux, A. Bousseksou, R. Lescouezec. *RSC Adv.* **2016**, *6*, 17456-17459.

[20] L. Alcázar, G. Aullón, M. Ferrer, M. Martínez. *Chem. Eur. J.* **2016**, *22*, 15227-15230.

[21] P. V. Bernhardt, M. Martínez. *Inorg. Chem.* **1999**, *38*, 424-425.

[22] P. V. Bernhardt, B. P. Macpherson, M. Martínez. *Inorg. Chem.* **2000**, *39*, 5203-5208.

[23] P. V. Bernhardt, F. Bozoglián, B. P. Macpherson, M. Martínez. *Dalton Trans.* **2004**, 2582-2587.

[24] P. V. Bernhardt, F. Bozoglián, B. P. Macpherson, M. Martínez. *Coord. Chem. Rev.* **2005**, *249*, 1902-1916.

[25] P. V. Bernhardt, F. Bozoglián, G. González, M. Martínez, B. P. Macpherson, B. Sienra. *Inorg. Chem.* **2006**, *45*, 74-82.

[26] P. V. Bernhardt, M. Martínez, C. Rodríguez. *Inorg. Chem.* **2009**, *48*, 4787-4797.

[27] P. V. Bernhardt, M. Martínez, C. Rodríguez. *Eur. J. Inorg. Chem.* **2010**, 5621-569.

[28] P. V. Bernhardt, M. Martínez, C. Rodríguez, M. Vazquez. *Inorg. Chem.* **2011**, *50*, 1429-1440.

[29] H. Oshio, H. Onodera, O. Tamada, H. Mizutani, T. Hikichi, T. Ito. *Chem. Eur. J.* **2000**, *6*, 2523-2530.

[30] Y. Z. Zhang, P. Ferko, D. Siretanu, R. Ababei, N. P. Rath, M. J. Shaw, R. Clérac, C. Mathonière, S. M. Holmes. *J. Am. Chem. Soc.* **2014**, *136*, 16854-16864.

[31] M. Nihei, Y. Sekine, N. Suganami, H. Oshio. *Chem. Lett.* **2010**, *39*, 978-979.

[32] J. Mercurol, Y. Li, E. Pardo, O. Risset, M. Seuleiman, H. Rousseliere, R. Lescouezec, M. Julve. *Chem. Commun.* **2010**, *46*, 8995-8997.

[33] M. Nihei, Y. Sekine, N. Suganami, K. Nakazawa, A. Nakao, H. Nakao, Y. Murakami, H. Oshio. *J. Am. Chem. Soc.* **2011**, *133*, 3592-3600.

[34] D. Siretanu, D. Li, L. Buisson, D. M. Bassani, S. M. Holmes, C. Mathonière, R. Clérac. *Chem. Eur. J.* **2011**, *17*, 11704-11708.

[35] L. Cao, J. Tao, Q. Gao, T. Liu, Z. Xia, D. Li. *Chem. Commun.* **2014**, *50*, 1665-1667.

[36] C. Zheng, J. Xu, Z. Yang, J. Tao, D. Li. *Inorg. Chem.* **2015**, *54*, 9687-9689.

[37] A. J. Bard, L. R. Faulkner. *Electrochemical Methods: Fundamentals and Applications,* Wiley, **2001**.

[38] P. V. Bernhardt, F. Bozoglián, B. P. Macpherson, M. Martínez, G. González, B. Sienra. *Eur. J. Inorg. Chem.* **2003**, 2512-2518.

[39] P. V. Bernhardt, F. Bozoglián, B. P. Macpherson, M. Martínez, A. E. Merbach, G. González, B. Sienra. *Inorg. Chem.* **2004**, *43*, 7187-7195.

[40] Maeder, M. and King, P. ReactLab. 2009. East Fremantle, WA. Australia, Jplus Consulting Pty Ltd.

[41] Binstead, R. A., Zuberbuhler, A. D., and Jung, B. SPECFIT32. 2005. Marlborough, MA, USA, Spectrum Software Associates.

[42] J. H. Espenson. *Chemical Kinetics and Reaction Mechanisms,* McGraw-Hill, **1981**.

[43] A. G. Lappin. *Redox Mechanisms in Inorganic Chemistry,* Ellis Horwood, **1994**.

[44] M. L. Tobe, J. Burgess. *Inorganic Reaction Mechanisms,* Longman, **1999**.

[45] Y. Ducommun, A. E. Merbach. Solvent Exchange Reactions*,* In: (Ed.: R. van Eldik), *Inorganic High Pressure Chemistry,* Elsevier, **1986**, pp. 69-114.

[46] D. A. Geselowitz, A. Hammershoi, H. Taube. *Inorg. Chem.* **1987**, *26*, 1842-1845.

[47] M. Martínez, M. A. Pitarque, R. van Eldik. *J. Chem. Soc. , Dalton Trans.* **1994**, 3159-3163.

[48] M. Martínez, M. A. Pitarque, R. van Eldik. *J. Chem. Soc. , Dalton Trans.* **1996**, 2665-2671.

[49] P. V. Bernhardt, M. A. Gonzálvez, M. Martínez. *Inorg. Chem.* **2017**, *56*, 14284-14290.

[50] M. T. Basha, J. Bordini, D. E. Richardson, M. Martínez, P. V. Bernhardt. *J. Inorg. Biochem.* **2016**, *162*, 326-333.

[51] P. V. Bernhardt, M. Martínez, C. Rodríguez, M. Vázquez. *Dalton Trans.* **2012**, *41*, 2122-2130.

[52] J. Garcia-Amoros, G. Stopa, G. Stochel, R. van Eldik, M. Martinez, D. Velasco. *Phys. Chem. Chem. Phys.* **2018**, *20*, 1286-1292.

[53] M. G. Basallote, P. V. Bernhardt, T. Calvet, C. E. Castillo, M. Font-Bardía, M. Martínez, C. Rodríguez. *Dalton Trans.* **2009**, 9567-9577.

[54] P. Atkins, T. Overton, J. Rourke, M. Weller, F. A. Armstrong. *Inorganic Chemsitry,* Oxford University Press, **2006**.

[55] D. D. Perrin. *Aust. J. Chem.* **1963**, *16*, 572-578.

[56] N. E. Good, G. D. Winget, W. Winter, T. N. Connolly, S. Izawa, R. M. M. Singh. *Biochem.* **1966**, *5*, 467-477.

[57] Frisch, M. J. and et al. Gaussian09. 2009. Wallingford CT, Gaussian Inc.

[58] A. D. Becke. *The Journal of Chemical Physics* **1993**, *98*, 5648-5652.

[59] B. Miehlich, A. Savin, H. Stoll, H. Preuss. *Chemical Physics Letters* **1989**, *157*, 200-206.

[60] C. Lee, W. Yang, R. G. Parr. *Phys. Rev. B* **1988**, *37*, 785-789.

[61] P. C. Hariharan, J. A. Pople. *Theoretica chimica acta* **1973**, *28*, 213-222.

[62] W. J. Hehre, R. Ditchfield, J. A. Pople. *The Journal of Chemical Physics* **1972**, *56*, 2257-2261.

[63] R. Ditchfield, W. J. Hehre, J. A. Pople. *The Journal of Chemical Physics* **1971**, *54*, 724-728.

[64] T. H. Dunning, P. J. Hay. *Modern Theoretical Chemistry,* (Ed.: H. F. Schaefer III), New York, Plenum, **1976**, pp. 1-28.

[65] D. J. Tannor, B. Marten, R. Murphy, R. A. Friesner, D. Sitkoff, A. Nicholls, B. Honig, M. Ringnalda, W. A. Goddard. *J. Am. Chem. Soc.* **1994**, *116*, 11875-11882.

[66] B. Marten, K. Kim, C. Cortis, R. A. Friesner, R. B. Murphy, M. N. Ringnalda, D. Sitkoff, B. Honig. *J. Phys. Chem.* **1996**, *100*, 11775-11788.

[67] A. V. Marenich, C. J. Cramer, D. G. Truhlar. *J. Phys. Chem. B* **2009**, *113*, 6378-6396.

[68] S. Grimme, J. Antony, S. Ehrlich, H. Krieg. *The Journal of Chemical Physics* **2010**, *132*, 154104.

[69] Bruker AXS Inc. SAINT. 2009.

[70] Shedrick, G. M. and Bruker AXS Inc. SADABS. 2008.

[71] G. M. Sheldrick. *Acta Cryst.* **2008**, *A64*, 112-122.

[72] T. J. Zerk, M. Martínez, P. V. Bernhardt. *Inorg. Chem.* **2016**, *55*, 9848-9857.

[73] M. Crespo, M. Martínez, S. M. Nabavizadeh, M. Rashidi. *Coord. Chem. Rev.* **2014**, *279*, 115-140.

Kinetico-mechanistic study of the redox pH cycling processes occurring on a robust water soluble cyanido-bridged mixed valence $\{Co^{III}/Fe^{II}\}_2$ square

Laura Alcázar,[a] *Paul V. Bernhardt,*[b] *Montserrat Ferrer,*[a] *Mercè Font-Bardia,*[c] *Albert Gallen,*[a] *Jesús Jover,*[a] *Manuel Martínez,*[*a] *Jack Peters*[a] *and Timothy J. Zerk*[b]

[a] Departament de Química Inorgànica i Orgànica, Secció de Química Inorgànica, Universitat de Barcelona, Martí i Franquès 1-11, E-08028 Barcelona, SPAIN.
e-mail: manel-martinez@qi.ub.es
[b] School of Chemistry and Molecular Biosciences, University of Queensland, Brisbane 4072, Queensland, Australia
[c] Unitat de Difracció de RX, Centres Científics i Tecnològics de la Universitat de Barcelona (CCiTUB), Universitat de Barcelona, Solé i Sabarís 1-3, E-08028-Barcelona, Spain

SUPPORTING INFORMATION

Table S1.- Values of the observed rate constants for the reaction of the mixed valence $\{Co^{III}/Fe^{II}\}_2^{2-}$ square with $S_2O_8^{2-}$ at different temperatures, pressures and pH(buffer) conditions ([square] ≈ 4×10^{-4} M; I = 1.0 M ($NaClO_4$)).

pH	T /ºC	P /atm.	$[S_2O_8^{2-}]$ / M	k_{obs1} / s^{-1}	k_{obs2} / s^{-1}
8.5 (Borax 0.025 M)	25	1	0.002	8.6×10^{-5}	1.2×10^{-5}
			0.005	1.9×10^{-4}	--
			0.008	3.8×10^{-4}	3.4×10^{-5}
			0.010	3.7×10^{-4}	4.6×10^{-5}
			0.015	5.4×10^{-4}	6.4×10^{-5}
			0.020	6.1×10^{-4}	7.9×10^{-5}
			0.025	7.0×10^{-4}	8.3×10^{-5}
			0.030	6.9×10^{-4}	9.0×10^{-5}
	35	1	0.002	2.8×10^{-4}	4.6×10^{-5}
			0.005	1.2×10^{-3}	6.4×10^{-5}
			0.010	1.9×10^{-3}	1.1×10^{-4}
			0.015	2.2×10^{-3}	1.6×10^{-4}
			0.025	2.4×10^{-3}	1.9×10^{-4}
			0.040	2.9×10^{-3}	2.6×10^{-4}
			0.050	3.0×10^{-3}	2.9×10^{-4}
	45	1	0.002	7.1×10^{-4}	3.8×10^{-5}
			0.005	1.9×10^{-3}	1.5×10^{-4}
			0.010	2.9×10^{-3}	3.3×10^{-4}
			0.015	3.7×10^{-3}	4.7×10^{-4}
			0.025	4.5×10^{-3}	6.3×10^{-4}
			0.030	4.6×10^{-3}	7.9×10^{-4}
			0.040	5.4×10^{-3}	7.9×10^{-4}
4.0 (PIPPS 0.25 M)	25	1	0.005	1.6×10^{-4}	4.6×10^{-5}
			0.010	--	8.4×10^{-5}
			0.015	3.3×10^{-4}	--
			0.020	3.5×10^{-4}	1.3×10^{-4}
			0.025	3.5×10^{-4}	1.3×10^{-4}
			0.030	3.8×10^{-4}	1.4×10^{-4}
	35	1	0.005	3.7×10^{-4}	1.1×10^{-4}
			0.010	6.7×10^{-4}	2.4×10^{-4}
			0.020	8.6×10^{-4}	3.3×10^{-4}
			0.030	--	3.9×10^{-4}
			0.040	1.0×10^{-3}	--
			0.050	1.0×10^{-3}	4.5×10^{-4}
	45	1	0.005	2.8×10^{-4}	3.4×10^{-4}
			0.010	1.8×10^{-3}	7.3×10^{-4}
			0.020	2.1×10^{-3}	1.1×10^{-3}
			0.030	--	1.2×10^{-3}
			0.040	2.9×10^{-3}	1.4×10^{-3}
			0.050	2.9×10^{-3}	--
2.0 (0.01 M $HClO_4$)	25	400	0.050	5.0×10^{-4}	3.5×10^{-4}
		700		1.1×10^{-3}	5.5×10^{-4}
		1000		2.0×10^{-3}	1.2×10^{-3}
		1300		2.1×10^{-3}	1.8×10^{-3}
		1600		4.0×10^{-3}	2.9×10^{-3}
		1800		5.2×10^{-3}	3.4×10^{-3}
1.5 (0.03 M $HClO_4$)	25	1	0.005	1.2×10^{-4}	2.9×10^{-5}
			0.010	2.0×10^{-4}	5.8×10^{-5}
			0.015	2.2×10^{-4}	7.7×10^{-5}
			0.020	2.5×10^{-4}	9.6×10^{-5}
			0.025	2.8×10^{-4}	9.7×10^{-5}
			0.030	2.8×10^{-4}	1.1×10^{-4}

	35	1	0.005	4.6×10^{-4}	4.2×10^{-5}
			0.010	6.3×10^{-4}	8.0×10^{-5}
			0.020	9.7×10^{-4}	1.9×10^{-4}
			0.030	1.2×10^{-3}	2.4×10^{-4}
			0.040	1.3×10^{-3}	2.6×10^{-4}
	45	1	0.050	--	2.9×10^{-4}
			0.005	1.5×10^{-3}	3.7×10^{-4}
			0.010	2.5×10^{-3}	9.0×10^{-4}
			0.020	3.3×10^{-3}	1.3×10^{-3}
			0.030	3.2×10^{-3}	1.6×10^{-3}
			0.040	4.3×10^{-3}	1.8×10^{-3}
			0.050	3.9×10^{-3}	1.8×10^{-3}
0 (1.0 M $HClO_4$)	15	1	0.0050	--	3.3×10^{-5}
			0.010	0.30	7.2×10^{-5}
			0.020	0.36	1.0×10^{-4}
			0.030	0.41	1.4×10^{-4}
			0.040	0.42	1.5×10^{-4}
			0.050	0.46	1.8×10^{-4}
	20	1	0.0050	0.34	3.0×10^{-4}
			0.010	0.38	5.2×10^{-4}
			0.020	0.47	7.3×10^{-4}
			0.030	0.56	--
		300		0.46	--
		600		0.56	--
		900		0.48	--
		1200		0.45	--
			0.037	--	8.4×10^{-4}
			0.040	0.53	--
			0.050	0.60	9.4×10^{-4}
			0.070	--	1.0×10^{-3}
		200		--	1.1×10^{-3}
		400		--	1.2×10^{-3}
		1000		--	1.4×10^{-3}
		1300		--	1.4×10^{-3}
		1600		--	1.5×10^{-3}
	30	1	0.0050	--	4.1×10^{-4}
			0.010	0.52	6.9×10^{-4}
			0.020	0.55	--
			0.030	0.64	1.2×10^{-3}
			0.040	0.65	1.2×10^{-3}
			0.050	0.67	1.8×10^{-3}
	35	1	0.0050	0.48	--
			0.010	0.63	--
			0.020	0.77	--
			0.030	0.86	--
			0.040	0.90	--
			0.050	0.95	--
	40	1	0.0050	--	7.0×10^{-4}
			0.010	--	2.0×10^{-3}
			0.020	--	3.1×10^{-3}
			0.030	--	4.0×10^{-3}
			0.040	--	4.5×10^{-3}
			0.050	--	4.4×10^{-3}

Table S2.- Values of the observed rate constants for the reaction of the oxidised $\{Co^{III}/Fe^{III}\}_2$ square with OH^- at different temperatures and $[OH^-]$(buffer) conditions ([square] ≈ 4×10^{-4} M; I = 1.0 M ($NaClO_4$)).

T /ºC	$[OH^-]$ / M	k_{obs1} / s^{-1}	k_{obs2} / s^{-1}
15	1×10^{-11} (PIPPS)	3.5×10^{-4}	5.0×10^{-7}
	1×10^{-10} (PIPPS)	4.8×10^{-4}	5.8×10^{-5}
	1×10^{-9} (MES)	2.0×10^{-3}	2.1×10^{-4}
	1×10^{-8} (MES)	3.1×10^{-3}	2.5×10^{-4}
	1×10^{-7} (MES)	3.5×10^{-3}	2.2×10^{-4}
	1×10^{-5} (HEPES)	7.5×10^{-3}	5.5×10^{-3}
	3.2×10^{-5} (CAPS)	5.4×10^{-2}	8.7×10^{-3}
	5.6×10^{-5} (CAPS)	6.0×10^{-2}	1.1×10^{-2}
	3.2×10^{-5} (CAPS)	5.4×10^{-2}	8.7×10^{-3}
	1.0×10^{-4} (CAPS)	5.9×10^{-2}	1.1×10^{-2}
	1.8×10^{-4} (CAPS)	6.6×10^{-2}	8.0×10^{-3}
	4.0×10^{-4} (CAPS)	5.6×10^{-2}	7.5×10^{-3}
	5.6×10^{-4} (CAPS)	4.0×10^{-2}	1.7×10^{-2}
	7.9×10^{-4} (CAPS)	5.8×10^{-2}	--
	1.0×10^{-3} (CAPS)	5.1×10^{-2}	--
	5.0×10^{-3} (NaOH)	27	3.1
25	1.0×10^{-12} (Chloroacetic acid)	No reaction	No reaction
	1×10^{-11} (PIPPS)	1.1×10^{-3}	1.0×10^{-6}
	1×10^{-10} (PIPPS)	1.3×10^{-3}	2.0×10^{-4}
	1×10^{-9} (MES)	6.0×10^{-3}	1.0×10^{-3}
	1×10^{-8} (MES)	1.2×10^{-2}	1.6×10^{-3}
	1×10^{-7} (MES)	1.2×10^{-3}	1.8×10^{-3}
	1×10^{-6} (CAPS)	2.7×10^{-2}	2.5×10^{-3}
	1×10^{-5} (CAPS)	3.6×10^{-2}	5.3×10^{-3}
	1×10^{-4} (CAPS)	1.2×10^{-1}	2.3×10^{-2}
	1×10^{-3} (CAPS)	1.5×10^{-1}	3.3×10^{-2}
	9.5×10^{-3} (NaOH)	53	9.6
	3.2×10^{-2} (NaOH)	70	10
	4.6×10^{-2} (NaOH)	48	6.3
35	1.0×10^{-12} (Chloroacetic acid)	No reaction	No reaction
	1×10^{-11} (PIPPS)	2.0×10^{-3}	1.7×10^{-6}
	1×10^{-9} (MES)	5.0×10^{-3}	7.5×10^{-4}
	1×10^{-7} (MES)	2.0×10^{-2}	2.3×10^{-3}
	1×10^{-4} (CAPS)	1.6×10^{-1}	4.5×10^{-2}
	2.0×10^{-3} (NaOH)	1.0×10^{1}	2.1
	5.0×10^{-3} (NaOH)	1.1×10^{1}	2.2
	8.0×10^{-3} (NaOH)	1.1×10^{1}	2,6
	1.1×10^{-2} (NaOH)	7.8	1.2
	1.4×10^{-2} (NaOH)	9.9	1.4
	1.7×10^{-2} (NaOH)	9.8	1.3

Table S3.- Crystal data and structure refinement for the *$(H_3O)_2[\{Co^{III}\{(Me)_2(\mu\text{-}ET)cyclen\}\}_2\{(\mu\text{-}NC)_2Fe^{II}(CN)_4\}_2].4HClO_4.9H_2O$* square mixed valence compound.

Empirical formula	**C36 H74 Cl4 Co2 Fe2 N20 O27**
Formula weight	1590.51
Temperature	100(2) K
Wavelength	0.71073 Å
Crystal system	Monoclinic
Space group	C 2/c
Unit cell dimensions	a = 28.454(6) Å
	b = 10.644(2) Å
	c = 21.226(4) Å
	α= 90.00(3) °
	β= 91.14(3) º
	γ = 90.00(3) °
Volume	6427(2) $Å^3$
Z	4
Density (calculated)	1.644 Mg/m^3
Absorption coefficient	1.210 mm^{-1}
F(000)	3280
Crystal size	0.477 x 0.198 x 0.178 mm^3
Theta range for data collection	2.794 to 30.582 °
Index ranges	-40<=h<=40, -15<=k<=15, -30<=l<=27
Reflections collected	126100
Independent reflections	9835 [R(int) = 0.0580]
Completeness to theta = 25.242°	99.6 %
Absorption correction	Semi-empirical from equivalents
Max. and min. transmission	0.7461 and 0.6550
Refinement method	Full-matrix least-squares on F^2
Data / restraints / parameters	9835 / 21 / 446
Goodness-of-fit on F^2	1.124
Final R indices [I>2sigma(I)]	R1 = 0.0619, wR2 = 0.1552
R indices (all data)	R1 = 0.0784, wR2 = 0.1634
Extinction coefficient	n/a
Largest diff. peak and hole	1.322 and -1.061 e.$Å^{-3}$
CCDC deposition number	1827523

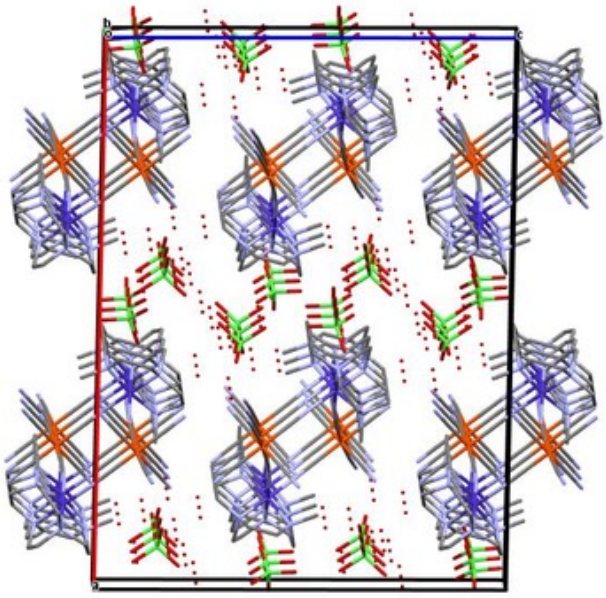

Figure S1.- Stacking of the anionic squares of the $\{Co^{III}/Fe^{II}\}_2^{2-}$complex forming columns along the b axis.

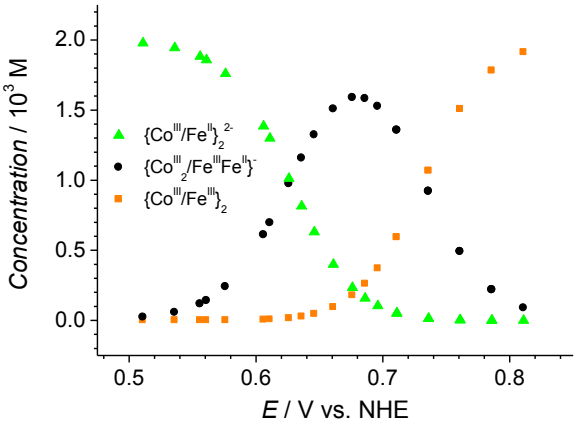

Figure S2.- Potential speciation plot for the series of $\{Co^{III}/Fe^{II}\}_2^{2-}$, $\{Co^{III}{}_2/Fe^{III}Fe^{II}\}^-$ and $\{Co^{III}/Fe^{III}\}_2$ complexes redox system.

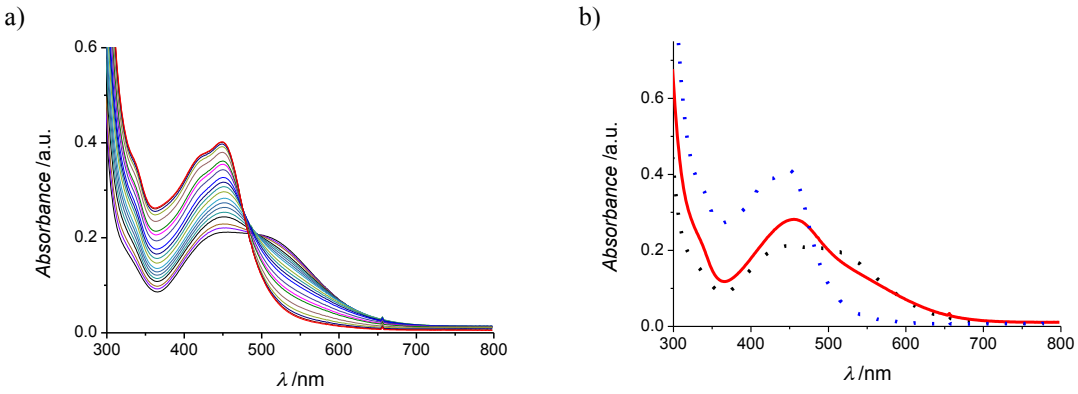

Figure S3.- a) Plot of the time-resolved spectra observed on the oxidation of a solution of the $\{Co^{III}/Fe^{II}\}_2^{2-}$ mixed valence square with peroxodisulfate at 25 ºC, pH = 1.50, I =1.0 M, total time 10 h. b) Specfit-calculated spectra of the intermediate species, $\{Co^{III}{}_2/Fe^{III}Fe^{II}\}^-$.

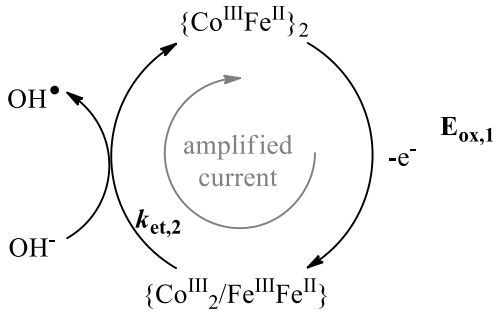

SCHEME S1

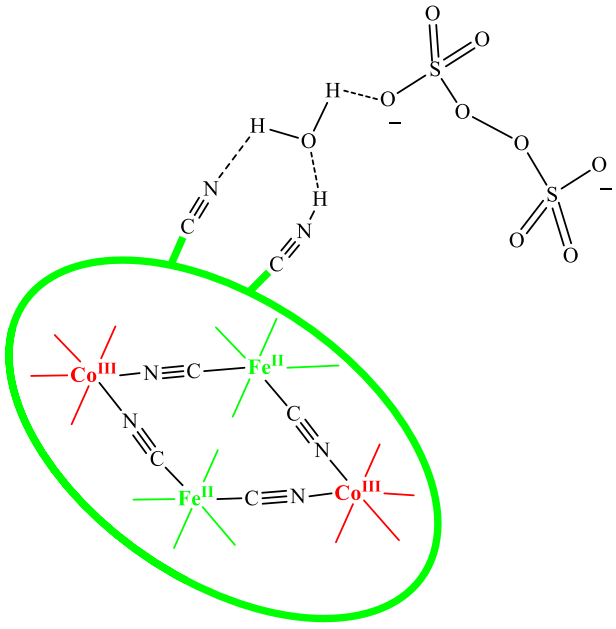

SCHEME S2

TOC

Bang it with $S_2O_8^{2-}$ from pH 0 to 14 in water, it stays there after oxidation of its iron moieties and returns to the original as soon as you increase to pH 3-4.